

# Effect of SiO<sub>2</sub> on the Crystallization Behaviors and In-Mold Performance of CaF<sub>2</sub>-CaO-Al<sub>2</sub>O<sub>3</sub> Slags for Drawing-Ingot-Type Electroslag Remelting



CHENG-BIN SHI, JING LI, JUNG-WOOK CHO, FANG JIANG, and IN-HO JUNG

The crystallization characteristics of CaF<sub>2</sub>-CaO-Al<sub>2</sub>O<sub>3</sub> slags with varying amounts of SiO<sub>2</sub> were experimentally studied. The effects of slag crystallization behaviors on the horizontal heat transfer and lubrication performance in drawing-ingot-type electroslag remelting (ESR) were also evaluated in terms of as-cast ingots surface quality and drawing-ingot operation. The results show that increasing SiO<sub>2</sub> addition from 0 to 6.8 mass pct strongly suppresses the crystallization of ESR type CaF<sub>2</sub>-CaO-Al<sub>2</sub>O<sub>3</sub> slags. The crystallization temperature of the studied slags decreases with the increase in SiO<sub>2</sub> addition. The liquidus temperatures of the slags also show a decreasing trend with increasing SiO<sub>2</sub> content. In CaF<sub>2</sub>-CaO-Al<sub>2</sub>O<sub>3</sub>-(SiO<sub>2</sub>) slags, faceted 11CaO·7Al<sub>2</sub>O<sub>3</sub>·CaF<sub>2</sub> crystals precipitate first during continuous cooling of the slag melts, followed by the formation of CaF<sub>2</sub> at lower temperatures. 11CaO·7Al<sub>2</sub>O<sub>3</sub>·CaF<sub>2</sub> was confirmed to be the dominant crystalline phase in the studied slags. CaF<sub>2</sub>-CaO-Al<sub>2</sub>O<sub>3</sub> slags with a small amount of SiO<sub>2</sub> addition are favorable for providing sound lubrication and horizontal heat transfer in mold for drawing-ingot-type ESR, which consequently bring the improvement in the surface quality of ESR ingot and drawing-ingot operating practice as demonstrated by plant trials.

DOI: 10.1007/s11663-015-0402-2

© The Minerals, Metals & Materials Society and ASM International 2015

## I. INTRODUCTION

SLAG plays an important role in electroslag remelting (ESR) process. The functions of the slag in ESR process are mainly to (I) generate Joule heat for melting electrode, (II) refine liquid metal such as absorption of non-metallic inclusions, desulfurization, *etc.*, (III) provide lubrication at copper mold/solidifying steel shell interface, (IV) serve as an insulation medium between mold and solidifying steel shell, and (V) control horizontal heat transfer between solidifying steel shell and mold. The inappropriate horizontal heat transfer through slag film and/or poor lubrication performance of slag generally results in unreliable operating practice during drawing-ingot-type ESR and surface defects on as-cast ingot. Horizontal heat transfer and lubrication performance of slag are strongly dependent on the crystallization characteristics of the slag.<sup>[1-6]</sup> Therefore,

it is required that ESR type slags possess proper crystallization properties to meet the requirements for heat transfer control and lubrication performance in drawing-ingot-type ESR process.

ESR slags generally are CaF<sub>2</sub>-CaO-Al<sub>2</sub>O<sub>3</sub>-based system with minor additions of MgO, TiO<sub>2</sub>, and/or SiO<sub>2</sub> to tailor the slag for the specific remelting requirements. The conventional slags used for electroslag remelting of superalloy are required to avoid the presence of SiO<sub>2</sub> in order to prevent the reaction between SiO<sub>2</sub> and strong oxidizing alloying elements such as Al and Ti. It is very difficult and costly to even keep extremely low SiO<sub>2</sub> content in ESR slags during practical slag manufacturing process due to the impurity in raw materials. For electroslag remelting of most steels, however, SiO<sub>2</sub> is a permissible constituent in the ESR slags.<sup>[7]</sup> In fact, it is suggested that a certain amount of SiO<sub>2</sub> addition into ESR type slags can meet several requirements of drawing-ingot-type electroslag remelting of steel for a given input power, such as improving lubrication performance, controlling silicon and aluminum contents in liquid steel, and modifying oxide inclusions type.

Many studies have been conducted to investigate the crystallization behaviors of conventional CaO-SiO<sub>2</sub>-CaF<sub>2</sub>-based slag system typically used for continuous casting mold fluxes.<sup>[8-15]</sup> The conventional such mold fluxes contain 70 mass pct (CaO + SiO<sub>2</sub>), 2 to 6 mass pct Al<sub>2</sub>O<sub>3</sub>, 2 to 10 mass pct Na<sub>2</sub>O (+ K<sub>2</sub>O), 0 to 10 mass pct F with varying addition of MgO, TiO<sub>2</sub>, B<sub>2</sub>O<sub>3</sub>, Li<sub>2</sub>O, *etc.*, and basicity (mass pct CaO/mass pct SiO<sub>2</sub>) of the fluxes ranges from 0.7 to 1.3.<sup>[4]</sup> In view of the significant difference in the slag chemistry, the crystallization

CHENG-BIN SHI, Assistant Professor, and JING LI, Professor, are with the State Key Laboratory of Advanced Metallurgy, University of Science and Technology Beijing (USTB), Beijing 100083, P.R. China. Contact e-mail: chengbin.shi@hotmail.com  
JUNG-WOOK CHO, Research Associate Professor, is with the Graduate Institute of Ferrous Technology, Pohang University of Science and Technology (POSTECH), Pohang 790-784, Republic of Korea. FANG JIANG, Principal Researcher, is with the Research Institute of Remelting Steels, Xingtai Iron and Steel Corp., Ltd., Xingtai 054027, P.R. China. IN-HO JUNG, Professor, is with the Department of Mining and Materials Engineering, McGill University, Montreal QC H3A 0C5, Canada. Contact e-mail: jungwook@postech.ac.kr

Manuscript submitted December 10, 2014.

Article published online June 24, 2015.

behaviors of ESR type  $\text{CaF}_2\text{-CaO-Al}_2\text{O}_3\text{-(SiO}_2\text{)}$  slags should be different from those of the mold fluxes. However, limited studies have been conducted to reveal the crystallization behaviors of  $\text{CaF}_2$ -containing slags with high  $\text{Al}_2\text{O}_3/\text{SiO}_2$  ratios.<sup>[14,16,17]</sup> Ryu *et al.*<sup>[14]</sup> studied the effect of  $\text{Al}_2\text{O}_3$  addition on the crystallization of  $\text{CaO-SiO}_2\text{-CaF}_2$  slag system, and found that the crystalline phase changed from  $3\text{CaO}\cdot 2\text{SiO}_2\cdot \text{CaF}_2$  to  $2\text{CaO}\cdot \text{SiO}_2\cdot \text{Al}_2\text{O}_3$  as  $\text{SiO}_2$  in the slag was substituted by  $\text{Al}_2\text{O}_3$ . Wang *et al.*<sup>[16]</sup> reported that the precipitation of  $\text{CaF}_2$  took place first in  $\text{CaO-Al}_2\text{O}_3$ -based slag system, followed by  $\text{NaCaAlSi}_2\text{O}_7$ , and later by  $\text{Al}_2\text{O}_3$  during solidification of the slag. Zhang *et al.*<sup>[17]</sup> reported that  $\text{Al}_2\text{O}_3$  played a key role in stabilizing  $\text{CaF}_2$  and consequently  $\text{CaF}_2$  precipitated during the cooling of slag melts when the mass ratio of  $\text{Al}_2\text{O}_3/\text{SiO}_2$  was above 0.84. Nevertheless, no experimental studies have been conducted for the crystallization characteristics of  $\text{CaF}_2\text{-CaO-Al}_2\text{O}_3$  slags with less than 10 mass pct of  $\text{SiO}_2$ . Furthermore, the thermochemical data for these slags are, to the best of the authors' knowledge, extremely scarce in literatures. Therefore, it is highly needed to ascertain the crystallization behaviors of  $\text{CaF}_2\text{-CaO-Al}_2\text{O}_3$  slags with a small amount of  $\text{SiO}_2$  addition for drawing-ingot-type ESR.

To achieve stable drawing-ingot operating practice and good surface quality of as-cast ingot, the effect of  $\text{SiO}_2$  on the crystallization characteristics of ESR type  $\text{CaF}_2\text{-CaO-Al}_2\text{O}_3$  slag was investigated by differential scanning calorimetry (DSC). The continuous cooling transformation (CCT) diagrams of crystalline phases were constructed. The crystalline phases in the solidified slags were identified by X-ray diffraction (XRD), and the microstructure and crystal compositions were determined by scanning electron microscope (SEM) equipped with energy dispersive X-ray spectroscopy (EDS). Furthermore, the effects of crystallization characteristics of  $\text{CaF}_2\text{-CaO-Al}_2\text{O}_3\text{-(SiO}_2\text{)}$  slags on their in-mold behaviors during drawing-ingot-type ESR were discussed based on plant trials.

## II. EXPERIMENTAL

### A. Sample Preparation

Slag samples were prepared with reagent-grade powders of  $\text{CaCO}_3$  ( $\geq 99.0$  mass pct),  $\text{SiO}_2$  ( $\geq 99.99$  mass pct),  $\text{CaF}_2$  ( $\geq 99$  mass pct), and  $\text{Al}_2\text{O}_3$  ( $\geq 99.99$  mass pct).  $\text{CaCO}_3$  powders were calcined at 1323 K (1050 °C) for 12 hours in a muffle furnace to produce CaO. It was confirmed from XRD identification, as shown in Figure 1, that the decomposition reaction of  $\text{CaCO}_3$  powders had completed thoroughly and the calcined products were CaO. A conventional ESR slag with an approximate composition of 31 mass pct  $\text{CaF}_2$ , 32 mass pct CaO, 33 mass pct  $\text{Al}_2\text{O}_3$ , and minor contents of other oxides, which is one of the widely used commercial slags for ESR operating in static mode, was selected as reference slag system in the current study. In the current study, the mass ratios of  $\text{CaF}_2/\text{CaO}/\text{Al}_2\text{O}_3$  were fixed at 1.0:1.0:1.0 in preparing  $\text{CaF}_2\text{-CaO-Al}_2\text{O}_3\text{-SiO}_2$  slags. The  $\text{SiO}_2$  content in the slags ranges from 0 to 9 mass

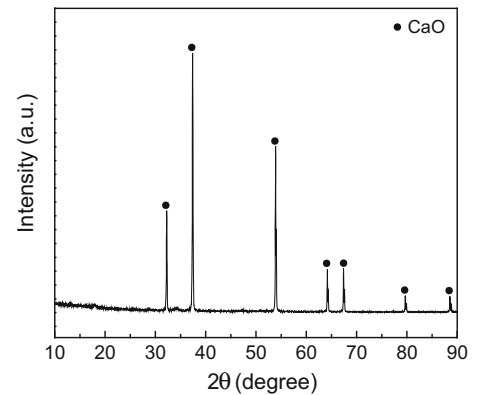


Fig. 1—XRD pattern of the calcined products of  $\text{CaCO}_3$  powders.

pct. The thoroughly mixed powders were melted at 1773 K (1500 °C) for 5 minutes in a graphite crucible to ensure complete melt and homogenization, and subsequently the liquid sample was quenched on a water-cooled copper plate. The quenched slag was then crushed and ground. The pre-melted slags were subjected to chemical analysis. The ion-selective electrode method was employed to determine fluorine content in the slag samples. The contents of calcium and aluminum in the slag were analyzed by inductively coupled plasma-atomic emission spectroscopy (ICP-AES). The gravimetric method was used to determine silica content in slag samples. The chemical compositions of the studied slag before and after pre-melting are listed in Table I. The chemical composition of pre-melted slag was used in describing the results of the current study.

### B. Experimental Procedure

#### 1. DSC measurement

Differential scanning calorimetry (DSC; Netzsch STA 449F3; Netzsch Instrument Inc., Germany) measurements were performed in Ar gas atmosphere (Ar gas flow rate at 60 mL/min) to investigate the crystallization characteristics of the slags. For each DSC measurement, approximately 40 mg of sample powders was heated at a constant heating rate of 25 K/min from room temperature up to 1663 K (1390 °C) in a platinum crucible with a diameter of 5 mm and a height of 5 mm, and held at this temperature for 3 minutes to eliminate bubbles and homogenize its chemical composition. Subsequently, the liquid sample was cooled at a constant cooling rate to the temperature below 473 K (200 °C). Four DSC measurements, continuous cooling rates of 5 K/min, 10 K/min, 15 K/min, and 20 K/min were performed for each slag sample, respectively. The DSC signal was recorded automatically during both heating and cooling cycles. The loss of slag sample was also recorded using thermal gravimetry (TG) during the DSC measurement. The weight loss was about 2.0 to 2.5 mass pct that occurred in DSC thermal history.

#### 2. SEM-EDS and XRD analysis

After DSC measurements, the slag samples were mounted with epoxy resin and polished. Then, a thin

**Table I. Chemical Compositions of the Studied Slag Before and After Pre-Melting (mass pct)**

Sample No.	Before Pre-melting				After Pre-melting			
	CaF <sub>2</sub>	CaO	Al <sub>2</sub> O <sub>3</sub>	SiO <sub>2</sub>	CaF <sub>2</sub>	CaO	Al <sub>2</sub> O <sub>3</sub>	SiO <sub>2</sub>
A	33.3	33.3	33.3	0.0	29.1	38.4	32.5	0.0
B	32.3	32.3	32.3	3.0	29.4	36.5	31.3	2.8
C	31.3	31.3	31.3	6.0	27.5	36.2	30.3	6.0
D	30.3	30.3	30.3	9.0	28.5	35.4	29.3	6.8

platinum film was coated onto the cross section of the polished sample to enhance the sample electric conductivity. The crystalline phases and crystal compositions of slag samples after DSC measurements were determined by SEM (FEI Quanta-250; FEI Corporation, Hillsboro, OR) equipped with EDS (XFlash 5030; Bruker, Germany).

To identify the crystalline phase corresponding to exothermic peak on DSC curves, a series of continuous cooling followed by quenching experiments were carried out to prepare slag sample for XRD analysis. Approximately 5 g of slag sample was melted in a graphite crucible at 1773 K (1500 °C) for 5 minutes, followed by a continuous cooling of liquid slag at a cooling rate of 10 K/min to the temperature below the crystallization end temperature corresponding to the second exothermic peak on DSC curve with the cooling rate of 10 K/min. Once reaching the desired temperature, the slag sample was quenched and the crystalline phases in the quenched samples were analyzed by XRD with Cu-K<sub>α</sub> radiation.

### III. RESULTS AND DISCUSSION

#### A. Crystalline Phase Formation

Figure 2 shows the DSC curves of slag samples at four different cooling rates, *i.e.*, 5 K/min, 10 K/min, 15 K/min, and 20 K/min, respectively. As shown in Figure 2, there are two exothermic peaks on DSC curves for each slag sample, indicating the occurrence of two successive crystallization events during continuous cooling process. The only exception was slag D at cooling rate of 20 K/min which showed a single exothermic peak. This result suggests that the crystallization of the first and second crystalline phases occurs in a narrow sequential process, or only single crystalline phase formation takes place from slag melt D at the cooling rate of 20 K/min. The crystallization event in slag D at the DSC cooling rate of 20 K/min will be further demonstrated from SEM-EDS analysis of the crystalline phases in the solidified slag in Section III-C. The exothermic peaks on DSC curves were designated as P1 and P2, respectively, according to the crystalline phase formation order in continuous cooling process. The DSC results show that the exothermic peaks on DSC curves shift toward lower temperatures with increasing the cooling rate.

XRD analysis was conducted to identify the crystalline phases in the quenched slag samples corresponding to the exothermic peaks on DSC curves shown in Figure 2. The XRD analysis results are presented in Figure 3. Two crystalline phases were identified in each slag sample by XRD, *i.e.*, 11CaO·7Al<sub>2</sub>O<sub>3</sub>·CaF<sub>2</sub> and CaF<sub>2</sub>. According to the phase diagram of the CaO-Al<sub>2</sub>O<sub>3</sub>-CaF<sub>2</sub> system by Nafziger,<sup>[18]</sup> the slag A should be crystallized first as 11CaO·7Al<sub>2</sub>O<sub>3</sub>·CaF<sub>2</sub>, and then CaF<sub>2</sub> can be formed. This crystallization sequence would not be changed with the addition of a small amount of SiO<sub>2</sub>. That is, it is believed that the first exothermic peak (higher temperature) and the second exothermic peak on DSC curves for slags A to D correspond to the crystallization of 11CaO·7Al<sub>2</sub>O<sub>3</sub>·CaF<sub>2</sub> and CaF<sub>2</sub>, respectively.

#### B. Crystallization Temperatures and Crystallization Ability of ESR Slags

The crystallization temperature of slag melt corresponds to the temperature at which the crystallization just begins in non-isothermal crystallization process. The determination of the crystallization temperature of crystalline phases from DSC curves has been illustrated in detail elsewhere.<sup>[19]</sup> The crystallization temperature combined with the time-temperature profiles recorded in DSC measurement were used to construct CCT diagrams of crystalline phases in the slags for the cooling rates of 5 K/min, 10 K/min, 15 K/min, and 20 K/min to reveal the crystallization tendency of the slags, as shown in Figure 4. It is observed that the crystallization temperatures of the crystalline phases in each slag sample decrease with the increase in continuous cooling rates in DSC measurements. This is attributed to the decrease in the available time for nucleation to proceed from slag melt as the continuous cooling rate increases. Crystallization consists of both nucleation and crystal growth processes which are strongly dependent on temperature. The nucleation and crystal growth rate as a function of temperature are schematically presented in the previous study.<sup>[20]</sup> Nucleation can be partially or totally suppressed when slag is cooled from melt at a higher cooling rate. When a slag sample is cooled from melt at a higher cooling rate, more available time is required for initiating nucleation from the melt. Consequently, the crystallization temperature of slag melt correspondingly decreases with increasing the continuous cooling rate.

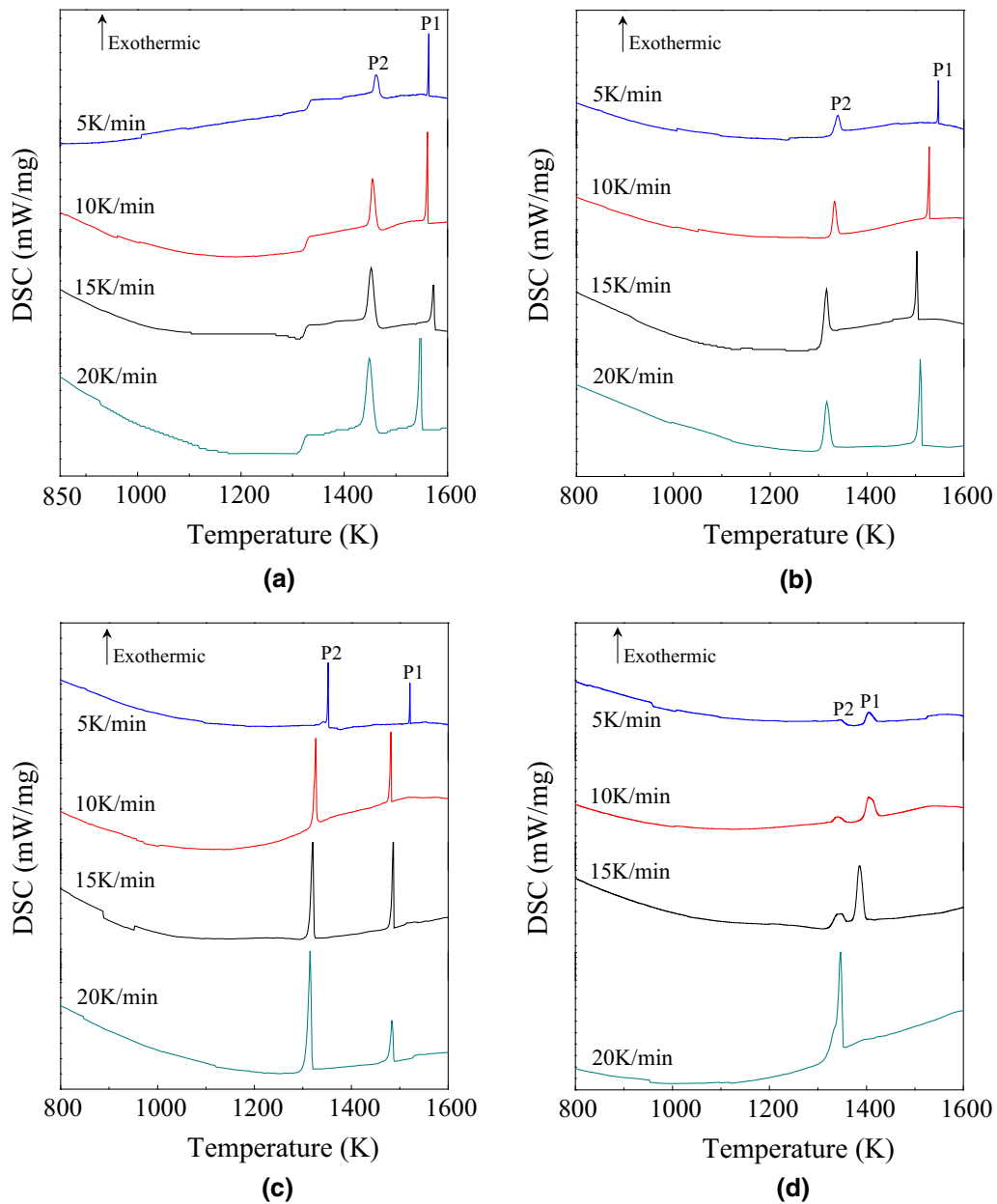


Fig. 2—DSC curves of non-isothermal crystallization of slag melts at various cooling rates: (a) slag A, (b) slag B, (c) slag C, (d) slag D.

The results obtained here are consistent with the findings for mold fluxes reported by the present authors.<sup>[19,21]</sup>

Figure 5 shows the CCT diagrams of the first and second crystalline phases precipitated from the slags containing different amounts of SiO<sub>2</sub>, respectively. The crystallization temperatures of the first crystalline phases 11CaO·7Al<sub>2</sub>O<sub>3</sub>·CaF<sub>2</sub> are observed to decrease with increasing SiO<sub>2</sub> contents in the slag, as shown in Figure 5(a). This may imply that SiO<sub>2</sub> reduces the activity of CaO in the slag to retard the crystallization of 11CaO·7Al<sub>2</sub>O<sub>3</sub>·CaF<sub>2</sub>. This result is also in accordance with the findings that the crystallization temperatures of CaO-SiO<sub>2</sub>-CaF<sub>2</sub>-based mold fluxes decrease with the

decrease in the mold flux basicity (mass pct CaO/mass pct SiO<sub>2</sub>).<sup>[9,21,22]</sup> It is clear from Figure 5(b) that the crystallization temperature of the second crystalline phase CaF<sub>2</sub> in the SiO<sub>2</sub>-free slag is much higher than those in the SiO<sub>2</sub>-containing slags. For CaF<sub>2</sub>-CaO-Al<sub>2</sub>O<sub>3</sub>-SiO<sub>2</sub> slags, it appears that increasing SiO<sub>2</sub> addition from 2.8 to 6.8 mass pct has no noticeable effect on the crystallization temperature of the second crystalline phase formed in these slags, as shown in Figure 5(b). The decrease in the crystallization temperature of ESR slags is correlated to the polymerization of the slag structure by SiO<sub>2</sub> addition. The further discussion will be presented from the view point of the polymerization of the slag structure.



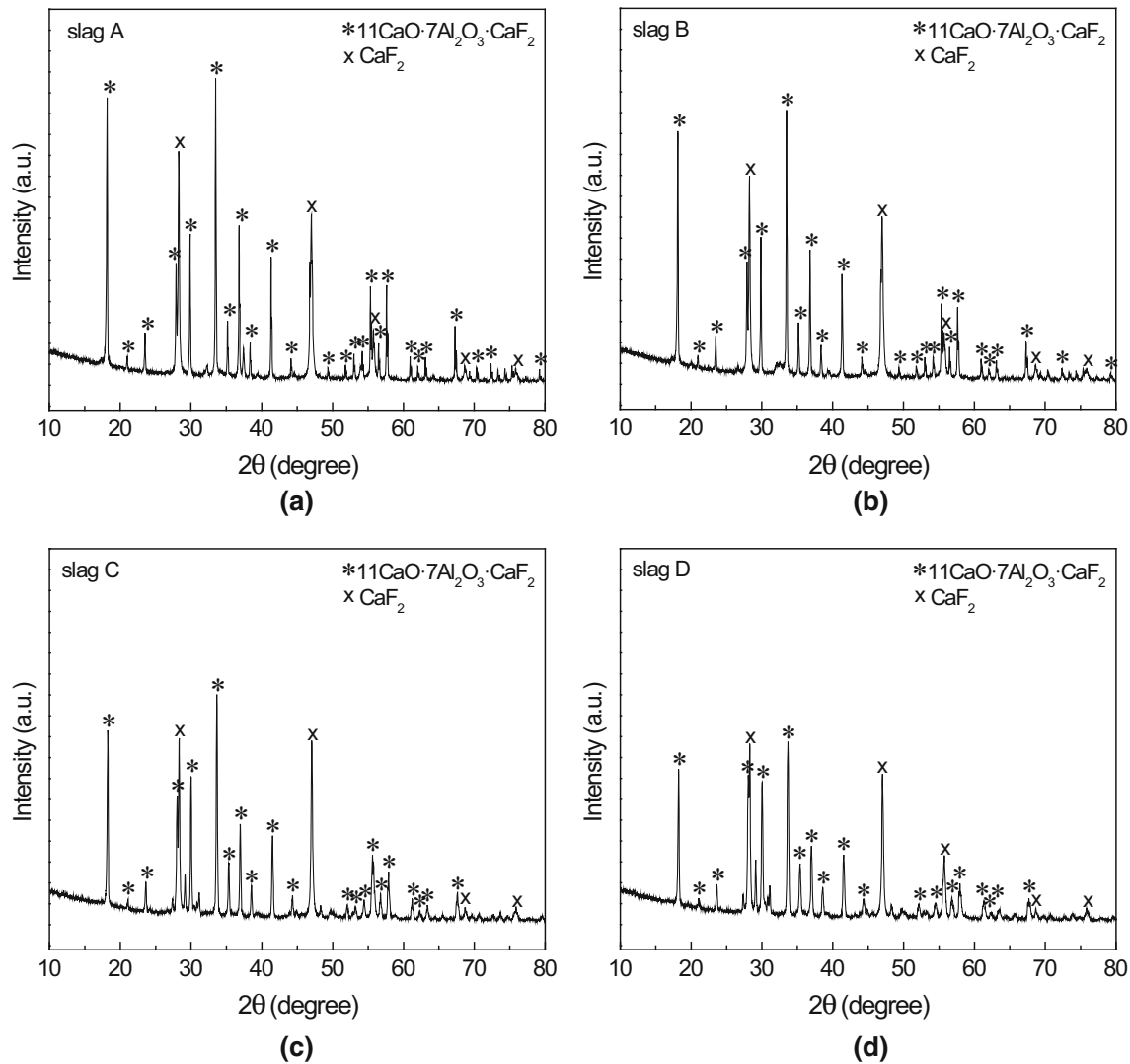


Fig. 3—XRD patterns of the slag quenched from the temperatures below the crystallization end temperatures corresponding to the cooling rate of 10 K/min: (a) slag A, (b) slag B, (c) slag C, (d) slag D.

The undercooling of slag melt crystallization can be employed to evaluate the crystallization ability of the slag. In order to reveal the degree of the undercooling, it is essential to know the equilibrium liquidus temperature of each slag. The calculated liquidus temperature of each slag is listed in Table II. In the calculation, the crystallization temperature of slag for the cooling rate 0 K/min was extrapolated from the primary crystallization temperatures obtained at different DSC cooling rates, and this crystallization temperature at 0 K/min is considered as liquidus. It can be seen that the liquidus temperatures of  $\text{CaF}_2\text{-CaO-Al}_2\text{O}_3$  slags decrease with increasing  $\text{SiO}_2$  addition from 0 to 6.8 mass pct. The undercooling was calculated by subtracting the crystallization starting temperature of the slag at various cooling rates from its liquidus temperature. Figure 6 shows the undercooling of slag melt crystallization. It is noted that the

undercooling of slag melt crystallization increases with increasing  $\text{SiO}_2$  addition in  $\text{CaF}_2\text{-CaO-Al}_2\text{O}_3$  slags, except for a few cases for slag C. It indicates that the crystallization ability of the  $\text{CaF}_2\text{-CaO-Al}_2\text{O}_3$  slags decreases with increasing  $\text{SiO}_2$  contents. This agrees well with the previous observations for  $\text{CaO-SiO}_2\text{-CaF}_2$ -based mold fluxes.<sup>[22]</sup> For the same slag sample, increasing the continuous cooling rate induces the increase in the undercooling for slag melt crystallization. This trend suggests that the increase in continuous cooling rate suppresses the crystallization of the slag melt.

The depolymerization degree of slag can be expressed in terms of the ratio of the number of non-bridging oxygen to tetrahedrally-coordinated atom. As a measure of depolymerization of slag melt, non-bridging oxygen per tetrahedrally-coordinated atom NBO/T can be calculated using the following equation<sup>[4]</sup>

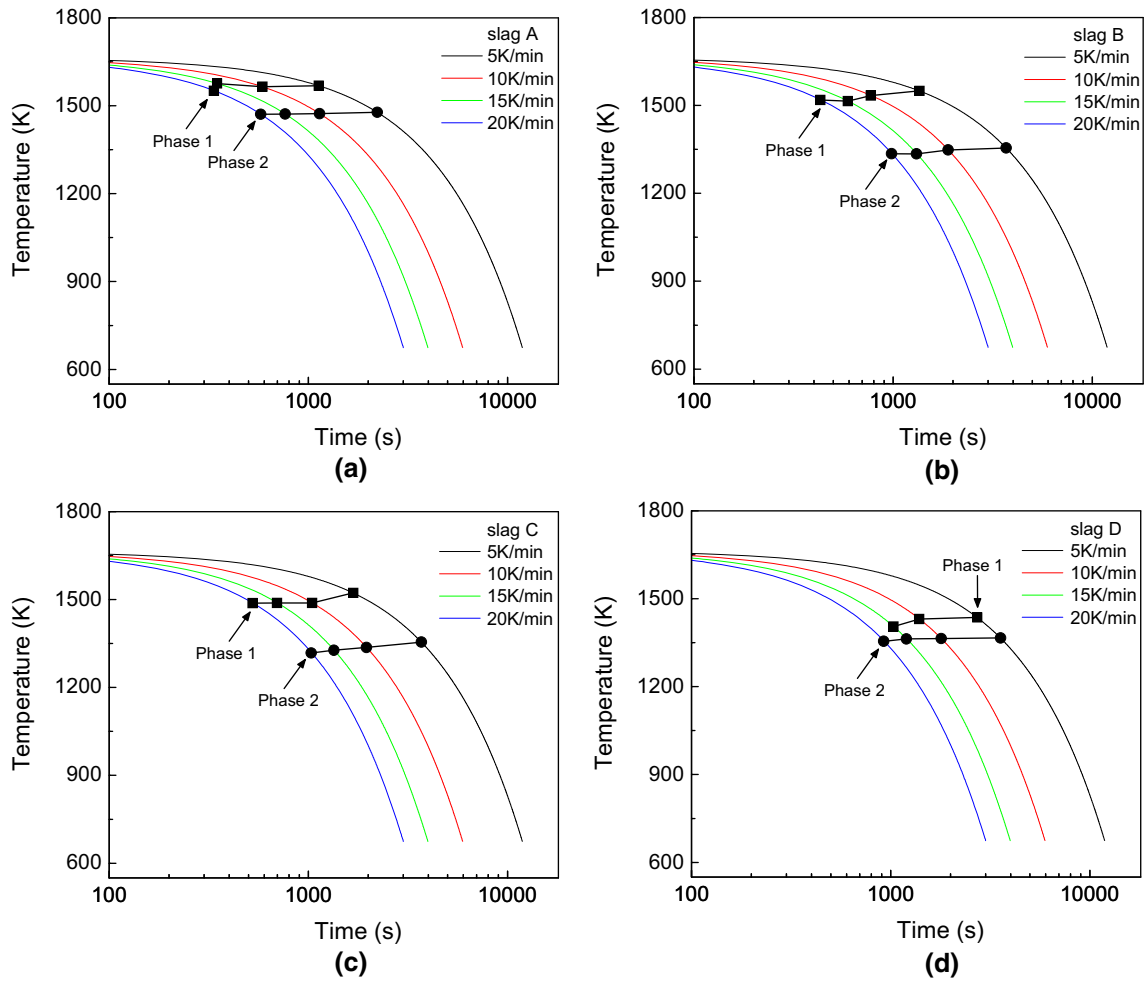


Fig. 4—CCT diagrams of slag melts: (a) slag A, (b) slag B, (c) slag C, (d) slag D.

$$\text{NBO/T} = \frac{2x_{\text{CaO}} + 2x_{\text{BaO}} + 2x_{\text{CaF}_2} + 2x_{\text{Na}_2\text{O}} - 2x_{\text{Al}_2\text{O}_3} + 6x_{\text{Fe}_2\text{O}_3} + (2x_{\text{MgO}} + 2x_{\text{MnO}})}{x_{\text{SiO}_2} + 2x_{\text{Al}_2\text{O}_3} + x_{\text{TiO}_2} + 2x_{\text{B}_2\text{O}_3} + (x_{\text{MgO}} + x_{\text{MnO}})}, \quad [1]$$

where  $x$  is the mole fraction of the component in slag. The calculated values of NBO/T for slag A, slag B, slag C, and slag D are 2.32, 2.19, 2.02, and 2.07, respectively. It suggests that increasing  $\text{SiO}_2$  addition in the slag with similar mass ratios of other components lowers the depolymerization degree of slag structures, which consequently makes the structural units of slag melts more complex, resulting in the increase in the diffusion resistance of slag components and energy barrier for crystallization. This can demonstrate the trends that the crystallization tendency of  $\text{CaF}_2$ - $\text{CaO}$ - $\text{Al}_2\text{O}_3$  slags decrease with increasing  $\text{SiO}_2$  addition in the slag.

### C. SEM-EDS Observation of Crystals and Their Morphologies

The morphologies of crystals and their compositions in the solidified slag melts after DSC measurements were determined by SEM-EDS. Combining SEM-EDS with XRD results, the crystalline phases could be identified. Figures 7(a) through (d) show the SEM back-scattered electron (BSE) images of slag after DSC measurements at continuous cooling rate of 10 K/min. SEM-EDS analysis revealed that the slag samples with the same chemical compositions contained the identical types of crystals even using four different DSC continuous cooling rates, except

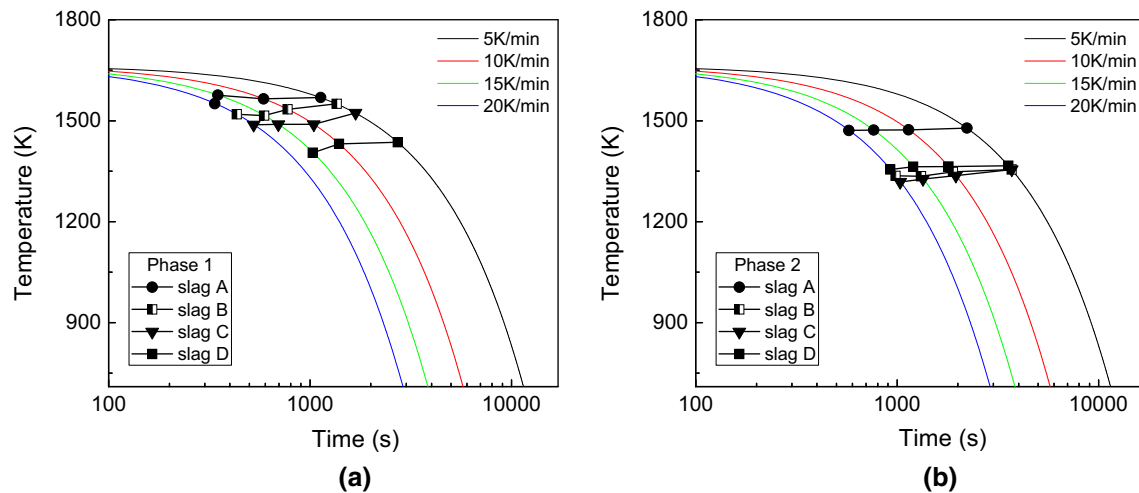


Fig. 5—CCT diagrams of crystalline phase formation in slag melts: (a) first crystalline phase  $11\text{CaO}\cdot 7\text{Al}_2\text{O}_3\cdot \text{CaF}_2$ , (b) second crystalline phase  $\text{CaF}_2$ .

**Table II. Liquidus Temperature of Slag and Calculated Values of NBO/T for Each Slag**

Sample No.	Liquidus Temperature* [K (°C)]	NBO/T
A	1576 (1303)	2.32
B	1558 (1285)	2.19
C	1524 (1251)	2.02
D	1474 (1201)	2.07

\*The liquidus temperature is the temperature obtained by extrapolating the crystallization temperatures of slag at cooling rates of 5 K/min, 10 K/min, 15 K/min, and 20 K/min to the value corresponding to the cooling rate of 0 K/min.

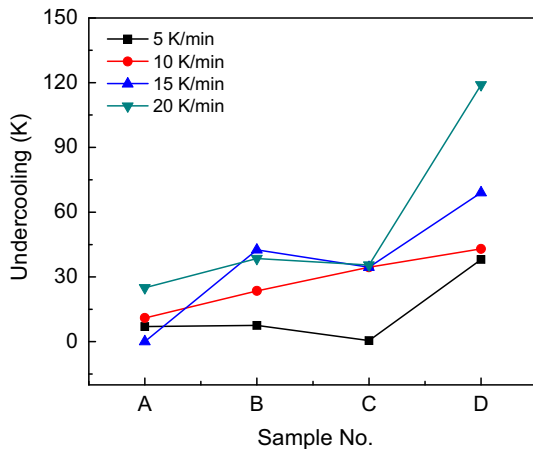


Fig. 6—Undercooling of slag melts crystallization at various cooling rates.

slag D with the constant cooling rate of 20 K/min. Therefore, only the SEM images of the slag samples with the DSC cooling rate of 10 K/min are presented in Figure 7.

A comparison of EDS and XRD results revealed that the dominant crystalline phase in ESR type  $\text{CaF}_2\text{-CaO-Al}_2\text{O}_3$  slags with different  $\text{SiO}_2$  content ranging from 0 mass pct to

6.8 mass pct was  $11\text{CaO}\cdot 7\text{Al}_2\text{O}_3\cdot \text{CaF}_2$  (designated as P1 in Figure 7). The morphology of  $11\text{CaO}\cdot 7\text{Al}_2\text{O}_3\cdot \text{CaF}_2$  crystals is faceted, and some of these faceted crystals are cube-like as shown in Figure 7. In addition, many  $\text{CaF}_2$  crystals were detected in each solidified slag sample (designated as P2 in Figure 7). The morphology of  $\text{CaF}_2$  crystals is near-spherical, while faceted  $\text{CaF}_2$  crystals were occasionally detected in each slag sample. No appreciable difference in the size of  $11\text{CaO}\cdot 7\text{Al}_2\text{O}_3\cdot \text{CaF}_2$  and  $\text{CaF}_2$  crystals can be observed, as shown in Figure 7. It was found that increasing  $\text{SiO}_2$  content did not change the morphologies of the crystals in these slags. The element mappings of the crystals in slag C shown in Figure 8 present the evidence of  $11\text{CaO}\cdot 7\text{Al}_2\text{O}_3\cdot \text{CaF}_2$  to be dominant crystalline phase, and the existence of  $\text{CaF}_2$  crystals in the slag.

Figures 9(a) and (b) show the BSE images of slag D after DSC measurement at cooling rate of 20 K/min. The crystals were identified as  $\text{CaF}_2$ . Unlike the phase formation in slag D that was continuously cooled at 5 K/min, 10 K/min, and 15 K/min, no crystalline phase  $11\text{CaO}\cdot 7\text{Al}_2\text{O}_3\cdot \text{CaF}_2$  was observed in crystallized slag D cooled at 20 K/min. This was the reason that only a single exothermic peak representing  $\text{CaF}_2$  formation was detected on DSC curve with the cooling rate of 20 K/min, as shown in Figure 2(d). It is concluded that the critical cooling rate for  $11\text{CaO}\cdot 7\text{Al}_2\text{O}_3\cdot \text{CaF}_2$  formation in slag D is between 15 K/min and 20 K/min. The precipitation of  $11\text{CaO}\cdot 7\text{Al}_2\text{O}_3\cdot \text{CaF}_2$  in  $\text{CaF}_2\text{-CaO-Al}_2\text{O}_3$  slags was inhibited with increasing  $\text{SiO}_2$  content up to 6.8 mass pct.

#### D. Evaluation of the In-Mold Performance of $\text{CaF}_2\text{-CaO-Al}_2\text{O}_3\text{-(SiO}_2\text{)}$ Slags During Drawing-Ingot-Type ESR

Unlike conventional ESR operating in a static mode, solidifying ingot is continuously drawn from the bottom of the mold during drawing-ingot-type ESR refining process, which closely resembles continuous casting process. For drawing-ingot-type ESR, slag is required to meet the demands in providing adequate lubrication

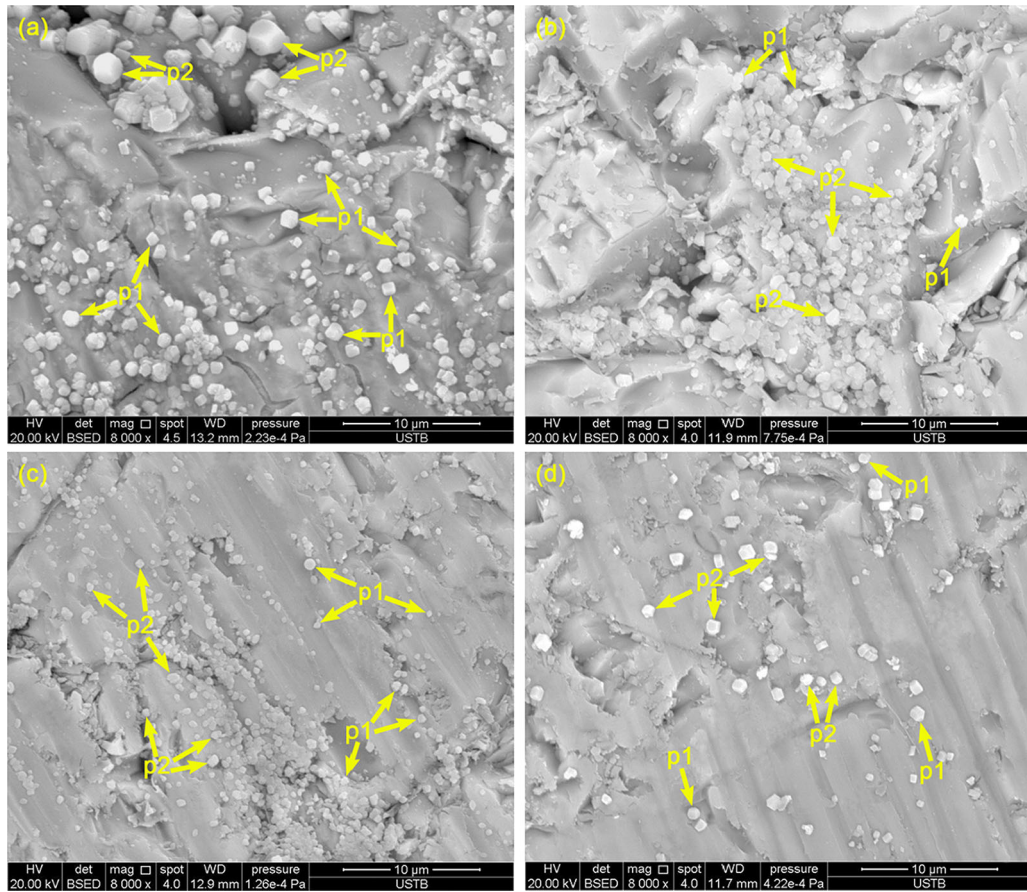


Fig. 7—BSE images of solidified slag cooled at 10 K/min: (a) slag A, (b) slag B, (c) slag C, and (d) slag D.

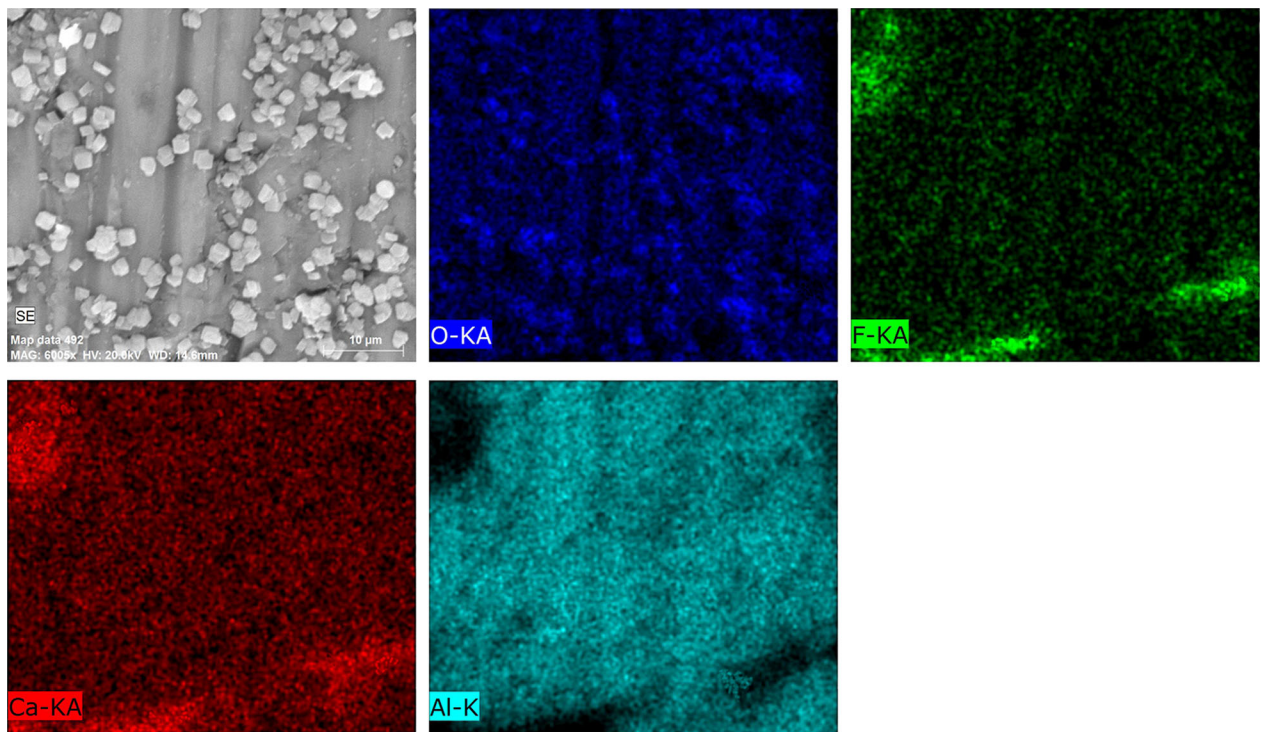


Fig. 8—Element mappings of crystals in solidified slag C after DSC measurement.



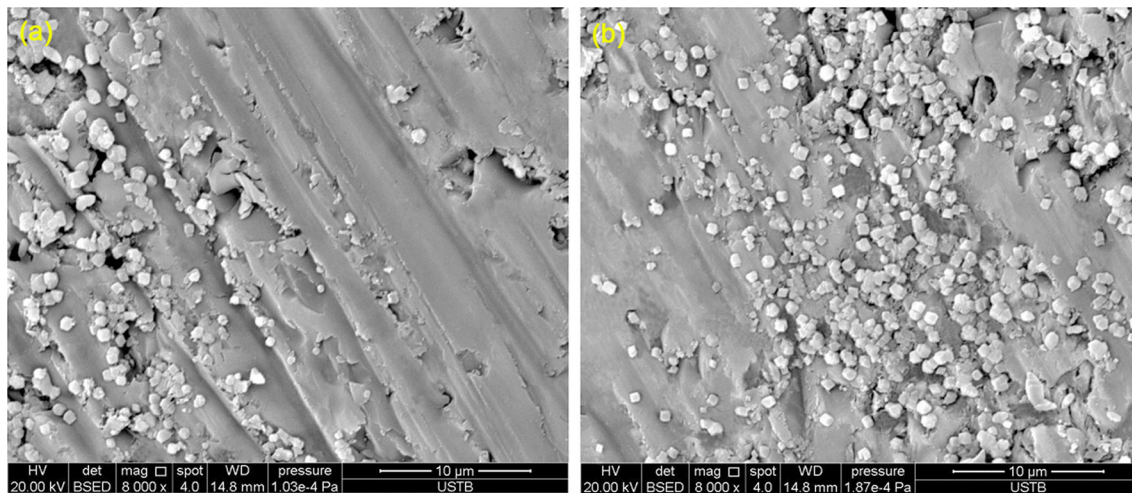


Fig. 9—BSE images of slag D after DSC measurement with a constant cooling rate of 20 K/min.

and controlling appropriate horizontal heat transfer across slag film in mold during refining process. Liquid slag gradually infiltrates into the channel between solidifying steel shell and copper mold forming a slag film during the ESR process. The slag film consists of a solid layer and a liquid layer next to steel shell. It is this slag film that plays a key role in controlling horizontal heat transfer in the mold and providing lubrication for drawing-ingot-type ESR, which will prevent the solidifying steel shell from adhering to the mold and provide good surface quality of as-cast ingot.

The solidification of liquid steel takes place against the slag film in mold in the ESR process. The friction between solidifying steel shell and slag film increases when using the slag with higher crystallization temperature for drawing-ingot-type ESR, which usually brings about the increase in the frequency of adherence occurrence of slag to the solidifying steel shell. With the increase in the crystallization temperature of slag, the thickness and hardness of solid slag film will increase. Under this condition, lubrication in the mold becomes poor, and initially solidified steel shell could be deformed during drawing-ingot-type ESR.

Moreover, the heat flux across the slag film decreases with the increase in the slag crystallization temperature, which gives rise to the increase in the surface temperature of steel shell and decrease in steel shell thickness. The mechanism of slag crystallization in reducing heat flux across slag film has been clarified in detail elsewhere.<sup>[23]</sup> Consequently, the strength of initially solidifying steel shell sharply decreases. This is unfavorable for the progress of initial solidification of molten steel in the mold near meniscus. As a consequence of insufficient lubrication and heat transfer induced by higher crystallization temperature of slag, defects arise near the meniscus and remain at the surface of the as-cast ESR ingots, such as streak marks, slag runner, and enclosed slag defect on ingot surface.

It has been ascertained in Section III-B that the increase of SiO<sub>2</sub> addition will cause the decrease in the slag crystallization temperature. The lower crystalliza-

tion temperature of slag is favorable for keeping adequate lubrication and horizontal heat flux in mold. It is considered that the present CaF<sub>2</sub>-CaO-Al<sub>2</sub>O<sub>3</sub> slag containing a small amount of SiO<sub>2</sub> can provide sound lubrication and heat transfer for drawing-ingot-type ESR, which brings the improvement in surface quality of as-cast ESR ingots. This has been confirmed by the observations of the surface appearance of H13 die steel ESR ingots (600 mm in diameter, 6 m in length), as shown in Figures 10 and 11.

Figures 10(a) and (b) present the photograph of as-cast ESR ingot produced by drawing-ingot-type protective gas ESR using the slag of 31 mass pct CaF<sub>2</sub>-32 mass pct CaO-33 mass pct Al<sub>2</sub>O<sub>3</sub> (close to slag A). It is clear from Figure 10 that there are many longitudinal streak marks across the ESR ingots surface produced with slag A, and many of these streak marks contain enclosed slag. The depth of these streak marks ranges between 3 and 6 mm (occasionally up to 10 mm). For the plant trials using slag A, it is frequently unstable in the *in situ* operation to draw the ingot from the mold during drawing-ingot-type ESR of H13 die steel. This is mainly attributed to the insufficient lubrication and heat transfer in the mold near meniscus provided by slag A during drawing-ingot-type ESR. Even though it was successful to draw the ingot from the bottom of the mold during ongoing ESR process, extensive surface grinding before subsequent forging processing was required to remove the streak marks and entrained macro-scale slag inclusions, which causes production yield losses and additional time-consuming grinding operation. Otherwise, the large streak marks and macro-scale slag inclusions enclosed in streak marks will serve as cracking initiation sites during forging of ESR ingots, which has been demonstrated in practical forging processing. The silicon content in as-cast ESR ingots was determined by the inductively coupled plasma-atomic emission spectroscopy (ICP-AES). It was found that the silicon content decreased from 1.02 mass pct in the consumable electrode to the average value of 0.80 mass pct in as-cast ingots after drawing-ingot-type ESR using slag A.

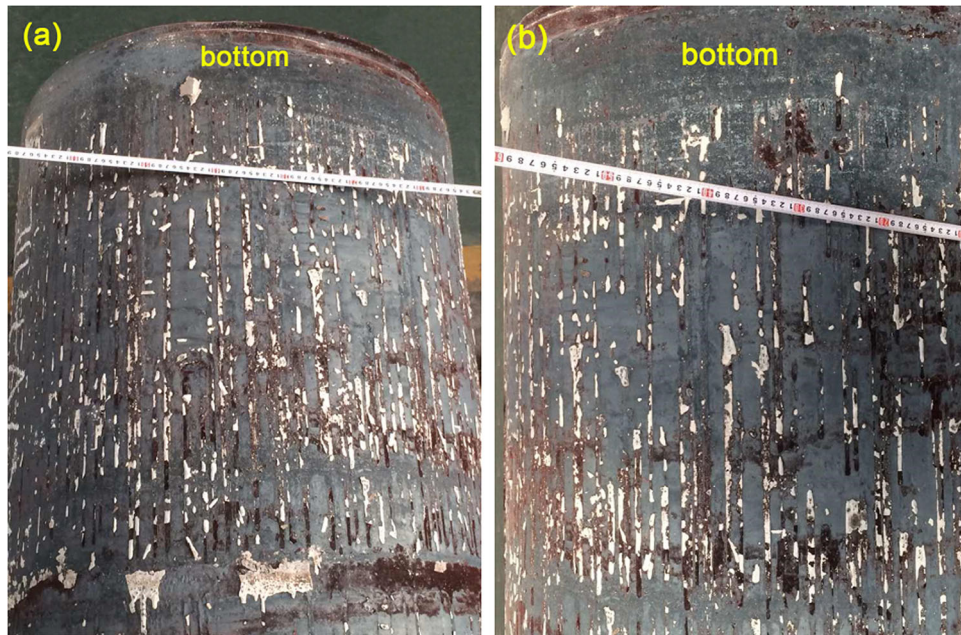


Fig. 10—Photograph of ESR ingots surface after drawing-ingot-type ESR trials using slag A. (Diameter: 600 mm, Length: 6 m).

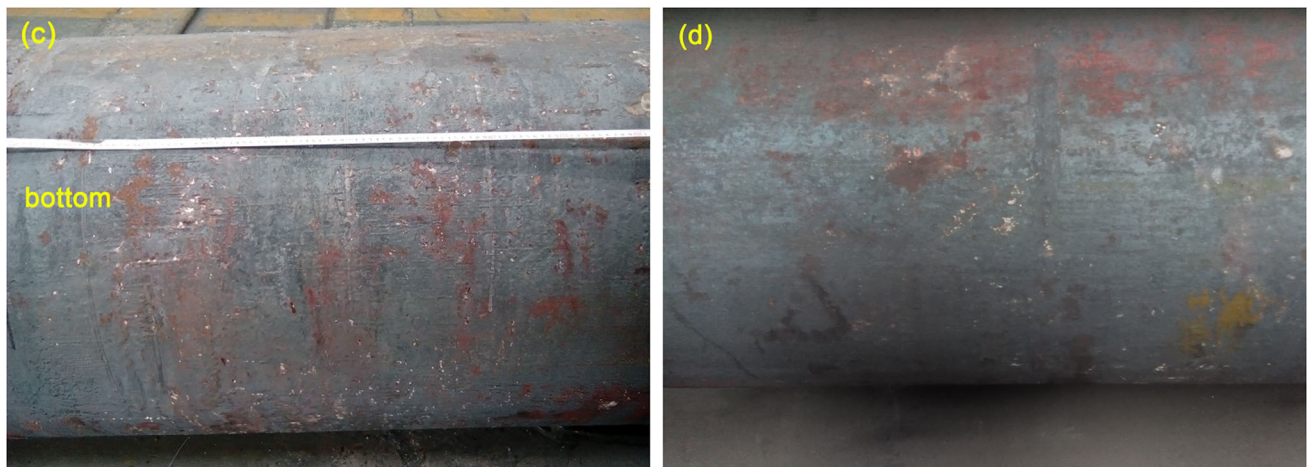


Fig. 11—Photograph of ESR ingots surface after drawing-ingot-type ESR trials using slag C. (Diameter: 600 mm, Length: 6 m).

Under the condition of the identical input power, virtually all streak marks on the ESR ingots surface have been eliminated when using slag C in ESR trials, as shown in Figure 11. The *in situ* drawing-ingot operation during protective gas ESR process was achieved successfully from plant trials using slag C. It suggests that slag C could provide adequate lubrication and heat flux in mold during drawing-ingot-type ESR. The plant trials showed that the silicon content remains relatively constant in H13 die steel before and after drawing-ingot-type protective gas ESR with  $\text{CaF}_2\text{-CaO-Al}_2\text{O}_3\text{-}$

$\text{SiO}_2$  slags. The silicon content in the as-cast ingots remelting with slag C is 1.02 mass pct.

The findings in the current work are expected to provide guiding basis for the design of slags for drawing-ingot-type ESR of steels, which are sensitive to the surface quality of ingot, oxide inclusion types, and/or variation in silicon and aluminum contents in steel. Considering the fact that the modification of oxide inclusions types can be achieved when using  $\text{SiO}_2$ -containing slags during ESR revealed by other researchers,<sup>[7,24]</sup> ongoing work regarding the effect of  $\text{SiO}_2$ -containing ESR slags on the oxide



inclusions in H13 die steel refined through drawing-ingot-type ESR is under progress.

#### IV. CONCLUSIONS

The crystallization behaviors of  $\text{CaF}_2\text{-CaO-Al}_2\text{O}_3\text{-(SiO}_2\text{)}$  slags were studied by DSC, XRD, and SEM-EDS. The effects of crystallization characteristics of  $\text{CaF}_2\text{-CaO-Al}_2\text{O}_3\text{-(SiO}_2\text{)}$  slags on their in-mold behaviors during drawing-ingot-type ESR were examined based on plant trials. The conclusions are summarized as follows:

- (1) The crystallization temperature and liquidus temperature of the slag decrease with increasing  $\text{SiO}_2$  content from 0 to 6.8 mass pct in  $\text{CaF}_2\text{-CaO-Al}_2\text{O}_3\text{-SiO}_2$  slags. The crystallization temperatures of the second crystalline phases formed in slag melts crystallization are not significantly affected by  $\text{SiO}_2$  addition ranging from 2.8 to 6.8 mass pct.
- (2) Increasing  $\text{SiO}_2$  addition strongly suppresses the crystallization of ESR type  $\text{CaF}_2\text{-CaO-Al}_2\text{O}_3$  slags, resulting from the decrease in the depolymerization degree of slag structures, which would bring an improvement in lubrication and horizontal heat transfer in mold.
- (3) In  $\text{CaF}_2\text{-CaO-Al}_2\text{O}_3$  slags containing varying  $\text{SiO}_2$  contents, the first crystalline phase precipitated during continuous cooling of the slag melts is  $11\text{CaO}\cdot 7\text{Al}_2\text{O}_3\cdot \text{CaF}_2$ , followed by  $\text{CaF}_2$  as the second crystalline phase. The dominant crystalline phase in  $\text{CaF}_2\text{-CaO-Al}_2\text{O}_3\text{-(SiO}_2\text{)}$  slags is confirmed to be  $11\text{CaO}\cdot 7\text{Al}_2\text{O}_3\cdot \text{CaF}_2$ , which is faceted in morphology. The morphology of  $\text{CaF}_2$  crystals is near-spherical, except for a few  $\text{CaF}_2$  crystals with faceted shape.
- (4) The  $\text{CaF}_2\text{-CaO-Al}_2\text{O}_3$  slags with a small amount of  $\text{SiO}_2$  addition are favorable for providing sound lubrication and horizontal heat transfer in mold during drawing-ingot-type protective gas ESR as indicated by the improvement in as-cast ingot surface quality and stable drawing-ingot operation, as well as for preventing the loss of silicon in steel from ESR plant trials.

#### ACKNOWLEDGMENTS

The sincere thanks from the author (C.B. SHI) are extended to senior engineers Zheng-xue Xue and Bao-shan

Guo of Xingtai Iron and Steel Corp., LTD for fruitful discussions on ESR plant trials. The authors are thankful to the financial support from the State Key Laboratory of Advanced Metallurgy, USTB (Grant No. 41603017). This work was also financially supported by the Fundamental Research Funds for the Central Universities (Grant No. FRF-TP-14-009A1), and China Postdoctoral Science Foundation (Grant No. 2014M560047).

#### REFERENCES

1. J.W. Cho, H. Shibata, T. Emi, and M. Suzuki: *ISIJ Int.*, 1998, vol. 38, pp. 268–75.
2. J.W. Cho, H. Shibata, T. Emi, and M. Suzuki: *ISIJ Int.*, 1998, vol. 38, pp. 440–46.
3. J.W. Cho, T. Emi, H. Shibata, and M. Suzuki: *ISIJ Int.*, 1998, vol. 38, pp. 834–42.
4. K.C. Mills, A.B. Fox, Z. Li, and R.P. Thackray: *Ironmak. Steelmak.*, 2005, vol. 32, pp. 26–34.
5. M. Hayashi, R.A. Abas, and S. Seetharaman: *ISIJ Int.*, 2004, vol. 44, pp. 691–97.
6. H. Nakada, M. Susa, Y. Seko, M. Hayashi, and K. Nagata: *ISIJ Int.*, 2008, vol. 48, pp. 446–53.
7. M. Allibert, J.F. Wadier, and A. Mitchell: *Ironmak. Steelmak.*, 1978, vol. 5, pp. 211–16.
8. Y. Kashiwaya, C.E. Cicutti, and A.W. Cramb: *ISIJ Int.*, 1998, vol. 38, pp. 357–65.
9. L. Zhou, W. Wang, F. Ma, J. Li, J. Wei, H. Matsuura F. Tsukihashi: *Metall. Mater. Trans. B*, 2012, vol. 43B, pp. 354–62.
10. J. Li, W. Wang, J. Wei, D. Huang, and H. Matsuura: *ISIJ Int.*, 2012, vol. 52, pp. 2220–25.
11. B. Lu, W. Wang, J. Li, H. Zhao, and D. Huang: *Metall. Mater. Trans. B*, 2013, vol. 44B, pp. 365–77.
12. T. Watanabe, H. Hashimoto, M. Hayashi, and K. Nagata: *ISIJ Int.*, 2008, vol. 48, pp. 925–33.
13. K. Tsutsumi, T. Nagasaka, and M. Hino: *ISIJ Int.*, 1999, vol. 39, pp. 1150–59.
14. H.G. Ryu, Z.T. Zhang, J.W. Cho, G.H. Wen, and S. Sridhar: *ISIJ Int.*, 2010, vol. 50, pp. 1142–50.
15. M. Hanao: *ISIJ Int.*, 2013, vol. 53, pp. 648–54.
16. W.L. Wang, K. Blazek, and A. Cramb: *Metall. Mater. Trans. B*, 2008, vol. 39B, pp. 66–74.
17. Z.T. Zhang, G.H. Wen, J.L. Liao, and S. Sridhar: *Steel Res. Int.*, 2010, vol. 81, pp. 516–28.
18. R.H. Nafziger: *High Temp. Sci.*, 1973, vol. 5, pp. 414–22.
19. C.B. Shi, M.D. Seo, J.W. Cho, and S.H. Kim: *Metall. Mater. Trans. B*, 2014, vol. 45B, pp. 1081–97.
20. C.B. Shi, M.D. Seo, H. Wang, J.W. Cho, and S.H. Kim: *Metall. Mater. Trans. B*, 2015, vol. 46B, pp. 345–56.
21. M.D. Seo, C.B. Shi, J.W. Cho, and S.H. Kim: *Metall. Mater. Trans. B*, 2014, vol. 45B, pp. 1874–86.
22. J.Y. Park, J.W. Ryu, and I. Sohn: *Metall. Mater. Trans. B*, 2014, vol. 45B, pp. 1186–91.
23. H. Nakada, M. Susa, Y. Seko, M. Hayashi, and K. Nagata: *ISIJ Int.*, 2008, vol. 48, pp. 446–53.
24. Z.B. Li, J.W. Zhang, and X.Q. Che: *J. Iron Steel Res.*, 1997, vol. 9, pp. 7–12.